


Article

# Agile Attitude Maneuver Control of Micro-Satellites for Multi-Target Observation Based on Piecewise Power Reaching Law and Variable-Structure Sliding Mode Control

Xinyan Yang, Yurong Liao, Lei Li and Zhaoming Li \* 

Department of Electronics and Optics, Space Engineering University, Beijing 101416, China; yangxyspace@163.com (X.Y.); yurongl6@163.com (Y.L.); lilspace@163.com (L.L.)

\* Correspondence: lizmspace@163.com

**Abstract:** This paper addresses the issue of agile attitude maneuver control for low-Earth-orbit satellites during short arc segments for multi-target observations. Specifically, a configuration design for Control Moment Gyroscopes (CMGs) and a hybrid control law are provided. The control law is adept at avoiding singularities and escaping singular planes. Subsequently, an optimal time-based attitude maneuver path-planning method is presented, rooted in the relationship between Euler angles/axis and quaternions. Furthermore, a novel satellite attitude maneuver controller is developed based on a piecewise power-reaching law for variable structure sliding mode control. The paper theoretically demonstrates that the proposed piecewise power reaching law possesses two favorable properties regarding convergence time. On the other hand, the designed reaching law maintains continuity at all stages, theoretically eliminating buffeting. The simulation results demonstrate that the proposed controller achieves an Euler angle control precision of  $\pm 0.03^\circ$  and angular velocity accuracy of  $\pm 0.15^\circ/s$ , fulfilling the demands of multi-objective observational tasks. Compared to conventional power reaching law controllers, the convergence time is reduced by 3 s, and Euler angle accuracy is improved by 70%. This underscores the effectiveness of the proposed algorithm.

**Keywords:** agile attitude control; piecewise power-reaching law; variable-structure sliding mode control; control moment gyroscopes; quaternions



**Citation:** Yang, X.; Liao, Y.; Li, L.; Li, Z. Agile Attitude Maneuver Control of Micro-Satellites for Multi-Target Observation Based on Piecewise Power Reaching Law and Variable-Structure Sliding Mode Control. *Appl. Sci.* **2024**, *14*, 797. <https://doi.org/10.3390/app14020797>

Academic Editor: Rosario Pecora

Received: 11 November 2023

Revised: 26 December 2023

Accepted: 15 January 2024

Published: 17 January 2024



**Copyright:** © 2024 by the authors. Licensee MDPI, Basel, Switzerland. This article is an open access article distributed under the terms and conditions of the Creative Commons Attribution (CC BY) license (<https://creativecommons.org/licenses/by/4.0/>).

## 1. Introduction

With the rapid development of aerospace technology, there has been an increasing demand for low-Earth-orbit micro-satellites to observe multiple targets during short arc segments continuously. The satellite is expected to quickly complete a large-angle agile attitude maneuver control for multi-target observation within a limited time frame. Such an agile attitude maneuver control for micro-satellites is typically achieved through large torque actuators like control moment gyroscopes (CMGs). On the other hand, research to improve the velocity of attitude maneuvering from a control algorithmic perspective is essential.

In the realm of controlling uncertain systems, the variable-structure sliding mode control has been the focus of research due to its high robustness and low dependence on model parameters. Therefore, it has found extensive application and development in controlling non-linear systems, such as robots [1], chaos systems [2], aerospace [3–5], and motors [6,7]. However, traditional sliding mode control faces serious issues of buffeting. In practical satellite attitude systems, buffeting not only causes energy waste, but also easily stimulates the flexible part of the satellite to oscillate, reducing the accuracy and stability of attitude control, and even leading to the failure of attitude control tasks. This has posed several difficulties for the application of sliding mode control. Therefore, how to mitigate or even eliminate buffeting has always been a focal point.

In order to suppress or eliminate buffeting, scholars have proposed methods such as boundary layer methods [8], terminal sliding mode control [9–11], high-order sliding mode control [12,13], and control methods based on reaching laws [14–18]. The boundary layer method employs saturation or continuous functions to replace the sign function, allowing the system to stay around the sliding mode plane. While this reduces buffeting, it also compromises control accuracy. High-order sliding mode control effectively eliminates buffeting, but obtaining the first derivative of the sliding variable is challenging. Terminal sliding mode control and reaching-law-based methods have similar mathematical structures, where the former focuses on the system's motion on the sliding mode plane, and the latter concentrates on the system's motion during the convergence phase. Current reaching laws are grouped into four types: constant-velocity reaching laws, exponential reaching laws, power-reaching laws, and general reaching laws. These have laid the foundation for the design of future reaching laws. Constant-velocity and exponential reaching laws encounter buffeting issues when the system reaches the sliding mode plane. Power reaching laws theoretically eliminate buffeting but have a slower convergence rate when distant from the sliding mode plane. In [19], the authors suggested fast power reaching laws, which combine exponential and power reaching laws to compensate for these defects. Moreover, in ref. [20], dual power reaching laws were introduced, further accelerating the approaching rate when far from the sliding mode plane. Additionally, ref. [21] developed a multi-power-reaching law that divides the approach phase into four stages, each featuring a high approaching rate. In [22], the authors designed a dual power composite function reaching law based on the final function, using the properties of the final function to speed up the approaching rate further.

This paper proposes a sliding mode variable-structure control method for satellite attitude maneuver based on piecewise power-law convergence law, aiming at the problem of multi-target-observation attitude maneuver control in the short arc segment of low-orbit satellites. This reaching law uses 1 as the dividing point to separate the convergence process into two phases. Utilizing the properties of power functions, the system has a substantial convergence rate in both phases, and the reaching law becomes zero at the equilibrium point. On the one hand, this accelerates the convergence rate, and theoretically, the proposed piecewise power reaching law exhibits two favorable properties in terms of convergence time. On the other hand, the designed reaching law maintains continuity at all stages, theoretically eliminating any buffeting. The reaching law also introduces two new linear terms, improving the algorithm's applicability under rapid attitude maneuver conditions. The effectiveness of the proposed algorithm is verified through simulation experiments.

The remainder of this paper is organized as follows: the attitude control system model is described in Section 2, the CMG model and the design of the control law are given in Section 3, the time-optimal path planning is introduced in Section 4, the sliding mode variable-structure controller based on the piecewise power reaching law is derived in Section 5, the simulation experiments and analysis are presented in Section 6, and the conclusions are drawn in Section 7.

## 2. Attitude Control System Model

### 2.1. Reference Coordinate System

Satellite body coordinate system  $Ox_b Y_b Z_b$ : The origin of the satellite body coordinate system is located on the center of mass of the satellite, and the three axes are consistent with the main axis of inertia of the satellite, firmly connected to the satellite.

Inertial coordinate system  $O_e X_i Y_i Z_i$ : The origin  $O_e$  is located at the center of the earth, the  $O_e X_i$  axis is in the equatorial plane, and the  $O_e Y_i$  axis points towards the infinite point on the intersection line between the equatorial plane and the ecliptic plane, which is also known as the direction of the vernal equinox. The direction of the  $O_e Z_i$  axis is consistent with the Earth's rotation axis; the  $O_e X_i$ ,  $O_e Y_i$ , and  $O_e Z_i$  axes form a right-handed orthogonal coordinate system.

### 2.2. Attitude Kinematics

A satellite’s attitude is generally determined by the orientation of its body coordinate system relative to the inertial coordinate system. There are various ways to describe this, with this paper relying on quaternions to describe micro-satellite attitudes. Meanwhile, the satellite attitude kinematics equations do not suffer from singularity issues regarding attitude quaternions. Moreover, the computational process involves only matrix multiplication operations and does not require complex trigonometric calculations. Therefore, this paper employs a satellite attitude kinematics model based on attitude quaternions to model the kinematic characteristics of the satellite.

The attitude quaternions are denoted by  $\mathbf{q} = \begin{pmatrix} q_0 \\ \mathbf{q}_v \end{pmatrix} = (q_0, q_1, q_2, q_3)^T$ , and the following equation provides the satellite attitude kinematics model:

$$\begin{cases} \dot{\mathbf{q}}_v = \frac{1}{2}(\mathbf{q}_v^\times + q_0 \mathbf{I}_3)\boldsymbol{\omega}_{ba} \\ \dot{q}_0 = -\frac{1}{2}\mathbf{q}_v^T \boldsymbol{\omega}_{ba} \end{cases} \quad (1)$$

where  $\mathbf{q}_v^\times = \begin{bmatrix} 0 & -q_3 & q_2 \\ q_3 & 0 & -q_1 \\ -q_2 & q_1 & 0 \end{bmatrix}$  represents the cross-product skew-symmetric matrix of  $\mathbf{q}_v$ , and  $\boldsymbol{\omega}_{ba}$  is the angular velocity of the satellite.

When the target desired quaternion  $\mathbf{q}_c$  and the initial quaternion  $\mathbf{q}_0$  are given, the error quaternion  $\mathbf{q}_e$  between the two is calculated using the following equation:

$$\mathbf{q}_e = \mathbf{q}_0^* \otimes \mathbf{q}_c \quad (2)$$

### 2.3. Attitude Dynamics

This paper focuses on micro-satellites. Generally, the solar panels of a micro-satellite are closely attached to its outer shell so that the micro-satellite can be treated as a rigid body. Hence, the satellite’s center of mass is chosen as the reference point. According to the angular momentum theorem, the time derivative of the angular momentum of the rigid satellite concerning its center of mass equals the external torque acting on the center of mass, i.e.,  $d\mathbf{H}_i/dt = \mathbf{T}$ . Here,  $\mathbf{H}_i$  represents the components of the angular momentum of the satellite concerning its center of mass in the inertial coordinate system, and  $\mathbf{T}$  is the external torque acting on the satellite’s center of mass.

The angular momentum is typically calculated in the satellite’s body coordinate system. Therefore, in the satellite’s body coordinate system, and based on the time derivatives of vectors in different coordinate systems, the dynamics can be expressed as follows:

$$\frac{d\mathbf{H}_b}{dt} + \boldsymbol{\omega}_{bi} \times \mathbf{H}_b = \mathbf{T} \quad (3)$$

where  $\boldsymbol{\omega}_{bi}$  are the components of the angular velocity vector of the satellite’s body coordinate system relative to the inertial coordinate system in the body coordinate system.  $\mathbf{H}_b = \mathbf{J}\boldsymbol{\omega}_{bi}$  represents the components of the angular momentum of the satellite about its center of mass in the body coordinate system, and  $\mathbf{J}$  is the total moment of inertia of the satellite.

Assuming that  $\mathbf{J}$  remains constant during the satellite’s rotation, then:

$$\frac{d\mathbf{H}_b}{dt} = \mathbf{J}\dot{\boldsymbol{\omega}}_{bi} \quad (4)$$

Considering that the micro-satellite body carries CMGs, let their total angular momentum be  $\mathbf{h}_b$ , and the installation matrix be  $\mathbf{C}$ . Equation (3) then becomes:

$$\mathbf{J}\dot{\boldsymbol{\omega}}_{bi} + \boldsymbol{\omega}_{bi} \times (\mathbf{J}\boldsymbol{\omega}_{bi} + \mathbf{C}\mathbf{h}_b) = -\mathbf{C}\frac{d\mathbf{h}_b}{dt} + \mathbf{T} \quad (5)$$

where  $-C\frac{dh_b}{dt}$  represents the control torque output by the CMGs.

The angular velocity error is denoted as  $\omega_e = \omega_{bi} - C_e\omega_r$ , where  $C_e = (q_{e0}^2 - q_{ev}^T q_{ev})I_3 + 2q_{ev}q_{ev}^T - 2q_{e0}q_{ev}^\times$  is the transformation matrix from the inertial coordinate system to the body coordinate system, and  $\omega_r$  is the desired angular velocity [23]. Substituting into Equation (5) yields the dynamics equation based on angular velocity error as follows:

$$J\dot{\omega}_e = -(\omega_e - C_e\omega_r) \times [J(\omega_e - C_e\omega_r) + Ch_b] + J(\omega_e \times C_e\omega_r - C_e\dot{\omega}_r) - C\frac{dh_b}{dt} + T \quad (6)$$

### 3. CMG Model and Control Law Design

Low-Earth-orbit micro-satellites must continuously observe multiple targets within short orbital arc segments. Therefore, the satellite must have a high maneuvering speed, which requires an actuation system capable of providing high-precision control torques. Hence, we chose the Single Gimbal Control Moment Gyro (SGCMG) as the satellite's actuation mechanism.

SGCMG comprises a low-speed gimbal and a high-speed rotor. The rotation axis of the low-speed gimbal is always perpendicular to that of the high-speed rotor. By imparting an angular velocity to the low-speed gimbal through the high-speed rotor's center of mass, the external gimbal's rotation can alter the internal rotor's angular momentum vector relative to the satellite. This produces an orthogonal output torque to both the rotor and gimbal axes. The relationship between the low-speed gimbal's angular velocity, the high-speed rotor's moment of inertia, and the output torque is described below.

$$T_{cmg} = -(\dot{\delta}x_g) \times (hz_g) = -\dot{\delta}hy_g \quad (7)$$

where  $T_{cmg}$  represents the SGCMG's output torque,  $\dot{\delta}$  denotes the low-speed gimbal's angular velocity,  $\delta$  is the angle through which the low-speed gimbal has rotated,  $h$  is the high-speed rotor's moment of inertia, and  $x, y, z$  are the three axes of the SGCMG's body coordinate system, coinciding with the gimbal axis, rotor axis, and the direction of the output torque, respectively.

When using CMG for attitude control, it is required that the designed control law has good maneuverability to drive the CMG group system to generate the desired torque. However, due to the presence of singular states, the design of the control law is more complex. In this study, low-orbit microsatellites continuously observe multiple targets within a short arc of passage, mainly maneuvering in the rolling axis direction. Therefore, satellites only need to have agile maneuverability in the rolling axis direction. The use of a full CMG configuration is not economically appropriate, which requires the design of a new control torque gyroscope configuration to achieve a maximum single-axis torque output, while the other two axes can be stably controlled through other actuators. The "scissors" configuration CMG is symmetrically installed through an even number of control moment gyroscopes, and the desired single-axis attitude maneuver control torque is reasonably coordinated between the CMGs. At the same time, the control law is used to keep the low-speed frame angle of the symmetrical CMG as synchronized as possible, avoiding disturbance torque in other directions. Therefore, in this study, we select two symmetrically installed scissor-configuration CMGs as the actuators, as illustrated in Figure 1.

The torques generated by CMG1 along the  $x$ -axis and  $y$ -axis are as follows:

$$\begin{cases} T_{1x} = -\dot{\delta}_1 h \cos \delta_1 \\ T_{1y} = -\dot{\delta}_1 h \sin \delta_1 \end{cases} \quad (8)$$

The torques generated by CMG2 along the  $x$ -axis and  $y$ -axis are as follows:

$$\begin{cases} T_{2x} = -\dot{\delta}_2 h \cos \delta_2 \\ T_{2y} = -\dot{\delta}_2 h \sin \delta_2 \end{cases} \quad (9)$$

When both CMG frames have equal angles and angular velocities, the control torques in the  $y$ -axis direction have an equal magnitude but in opposite directions, canceling each other. This will only generate a net torque along the  $x$ -axis, with a magnitude of:

$$T_x = -2\dot{\delta}_1 h \cos \delta_1 \tag{10}$$

Therefore, the control law for a single set of scissors-configured CMG1 is:

$$\dot{\delta}_{d1} = \frac{-T_{cmg}}{2h \cos \delta_1} \tag{11}$$

To ensure that the low-speed gimbal angles of the paired CMGs remain synchronized, a Proportional-Integral (PI) control is introduced, guaranteeing that the nominal gimbal angular velocity allocation operates under desired conditions. The low-speed gimbal angle of CMG2 follows that of CMG1:

$$\dot{\delta}_{d2} = \dot{\delta}_{d1} + K_p(\delta_1 - \delta_2) + K_I \int (\delta_1 - \delta_2) \tag{12}$$

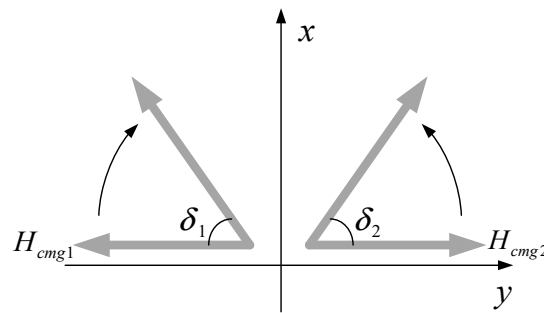


Figure 1. Typical installation schematic of scissors-type CMG.

#### 4. Time-Optimal Path Planning

Planning large-angle maneuvers for the satellite mainly involves two aspects, i.e., selecting the path for the satellite’s maneuvers to find the shortest distance for the satellite to travel along and planning the satellite’s angular velocity to minimize the time required for the maneuver.

Due to the maximum output torque of the satellite in the rolling axis direction and the fact that this direction is the main attitude maneuver direction during target observation, in order to achieve a large-angle rapid maneuver, the angular velocity in this direction should be able to quickly reach its maximum. Therefore, the trapezoidal path planning method is chosen, which requires that the angular velocity of the satellite maneuver should meet the following two conditions:

- (1) The satellite should perform rotational maneuvers around the Euler axis, i.e., the angular velocity direction should align with the Euler axis.
- (2) The satellite’s initial and final angular velocities should be zero. The change in the satellite’s angular velocity should go through three stages: uniform acceleration, uniform velocity, and uniform deceleration, as depicted in Figure 2. The size of the control torque limits the magnitudes of acceleration during the uniform acceleration and uniform deceleration stages. During the uniform velocity phase, the magnitude of the angular velocity is constrained by the maximum allowable rotational velocity, denoted as  $\omega_{max}$ .

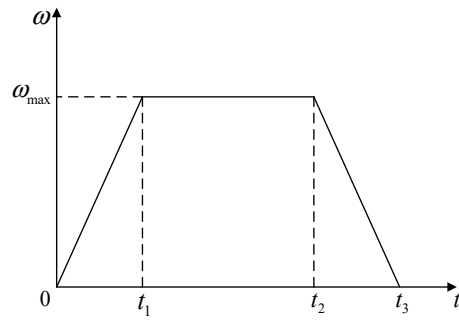


**Figure 2.** Large-angle maneuver angular velocity path planning.

Using Equation (2), the error quaternion is calculated based on the initial and desired quaternions:

$$\Delta q = q_c^* \otimes q_d \tag{13}$$

where  $\Delta q$  represents the error quaternion, signifying the difference between the initial and desired attitudes;  $q_c$  denotes the initial quaternion; and  $q_d$  is the desired quaternion.

Utilizing the relationship between the quaternion and Euler axis/angle, the Euler axis direction  $e = (e_x, e_y, e_z)^T$  and the Euler angle magnitude  $\Phi = 2\arccos(\Delta q_0)$  are calculated, where  $e_x = \Delta q_1 / \sin(\Phi/2)$ ,  $e_y = \Delta q_2 / \sin(\Phi/2)$ ,  $e_z = \Delta q_3 / \sin(\Phi/2)$ .

The satellite always moves in one direction, and the area of the trapezoid in Figure 2 represents the Euler angle  $\Phi$  of the satellite’s rotation.

$$\Phi = \frac{1}{2}a_\omega t_1^2 + \omega_{\max}(t_2 - t_1) + \frac{1}{2}a'_\omega (t_3 - t_2)^2 \tag{14}$$

where  $a_\omega$  and  $a'_\omega$  are the angular accelerations during the acceleration and deceleration phases, respectively. To minimize the time to the greatest extent possible, both are set to the maximum angular acceleration the satellite can provide. Therefore, they are equal in magnitude. To reduce the angular velocity to zero, the conditions are as follows:  $t_3 - t_2 = t_1$ ,  $t_1 = \omega_{\max} / a_\omega$ . Thus,  $\Phi = \omega_{\max} t_2$ , and consequently,  $t_2 = \Phi / \omega_{\max}$ ,  $t_3 = t_2 + t_1 = \Phi / \omega_{\max} + \omega_{\max} / a_\omega$ .

The expression for the change in Euler angles over time is:

$$\Phi(t) = \begin{cases} \frac{1}{2}a_\omega t^2 & 0 < t \leq t_1 \\ \omega_{\max} t_1 + \frac{1}{2}a_\omega t_1^2 & t_1 < t \leq t_2 \\ \Phi - \frac{1}{2}a_\omega (t_3 - t)^2 & t_2 < t \leq t_3 \end{cases} \tag{15}$$

When the maneuver angle of the satellite is not large, the angular velocity path does not include a uniform velocity phase. The angular velocity changes are illustrated in Figure 3. To bring the angular velocity to zero, the conditions are as follows:  $t'_2 - t'_1 = t'_1$ . Therefore  $\Phi = a_\omega t'^2_1$ , and, consequently,  $t'_2 = 2t'_1 = 2\sqrt{\Phi / a_\omega}$ .

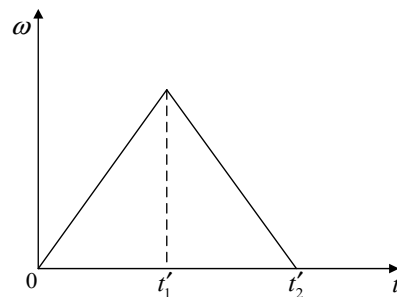


**Figure 3.** Angular velocity path planning without a uniform velocity phase.

The change in Euler angles over time is expressed as follows:

$$\Phi(t) = \begin{cases} \frac{1}{2}a_\omega t^2 & 0 < t < t'_1 \\ \Phi - \frac{1}{2}a_\omega (t'_2 - t)^2 & t'_1 \leq t \leq t'_2 \end{cases} \quad (16)$$

In scenarios with no uniform velocity phase, the maximum angle for the maneuver occurs at  $t'_1$  when the angular velocity is  $\omega_{\max}$ . At this point,  $\Phi_{\max} = \omega_{\max}t'_1 = \omega_{\max}^2/a_\omega$ . Therefore, if  $\Phi > \omega_{\max}^2/a_\omega$ , the angular velocity path includes a uniform velocity phase. If  $\Phi \leq \omega_{\max}^2/a_\omega$ , the angular velocity path does not include a uniform velocity phase. Based on the Euler angles at each moment in time, the corresponding error quaternion is calculated as follows:

$$\Delta q(t) = \left[ \cos \frac{\Phi(t)}{2}, e_x \sin \frac{\Phi(t)}{2}, e_y \sin \frac{\Phi(t)}{2}, e_z \sin \frac{\Phi(t)}{2} \right]^T \quad (17)$$

Therefore, the path of the satellite's attitude quaternion is as follows:

$$q(t) = q_c \otimes \Delta q(t) \quad (18)$$

## 5. Sliding Mode Variable-Structure Controller Based on Piecewise Power Reaching Law

### 5.1. Variable Structure Sliding Mode Control

For the attitude tracking model mentioned above, the traditional sliding surface is as follows:

$$S = \omega_e + kq_{ev} \quad (19)$$

where  $k$  is a positive constant.

To ensure  $\lim_{x \rightarrow 0} S\dot{S} < 0$ , let:

$$\dot{S} = -k_1 \text{sgn}(S) \quad (20)$$

Combining the kinematic and dynamic equations for satellite attitude tracking, the control torque for the satellite is given as:

$$u_c = \Gamma(\cdot) - k_1 J \text{sgn}(s) - k J \dot{q}_{ev} \quad (21)$$

where  $\Gamma(\cdot) = (\omega_e + D\omega_d)J(\omega_e + D\omega_d) + (\omega_e + D\omega_d)Ch_b - J(\omega_e^\times D\omega_d - D\dot{\omega}_d)$ .

### 5.2. Design of Piecewise Power Reaching Law

This paper proposes a new piecewise power reaching law to accelerate the convergence rate further. This law sets 1 as the boundary point and divides the approach into two phases:  $|S| \geq 1$  and  $|S| < 1$ . Utilizing the properties of power functions, the system has a high convergence rate in both phases, and the convergence rate at the equilibrium point ( $|S| = 0$ ) is zero.

The structure of the piecewise power reaching law is as follows:

$$\dot{S} = \begin{cases} -k_1 S - k_2 S^{\frac{p}{q}} & |S| \geq 1 \\ -k_3 S - k_4 S^{\frac{m}{n}} & |S| < 1 \end{cases} \quad (22)$$

where  $k_1, k_2, k_3, k_4 > 0$  and  $k_1 + k_2 = k_3 + k_4$ ,  $\frac{p}{q} > 1$ ,  $0 < \frac{m}{n} < 1$ , and  $p, q, m, n$  are all odd numbers.

Like general power laws, the designed reaching law is continuous at any stage and does not exhibit chattering theoretically. To allow for a flexible design of  $k_2$  and  $k_4$ , two linear terms are added (otherwise, to ensure the continuity of the reaching law  $k_2 = k_4$ , which restricts parameter selection).

From the expression of the approaching law, it can be seen that the motion process of the system is divided into two stages, far away from the sliding surface and near the

sliding surface. When moving away from the sliding surface, i.e.,  $|S| \geq 1$ , the approach law is dominated by the first term, and when approaching the sliding surface, i.e.,  $0 < |S| < 1$ , the approach law is dominated by the second term. From the properties of power functions, it can be inferred that the designed convergence law has a significant convergence rate at any stage. The design of a piecewise function has several advantages:

- (1) The system has a faster convergence rate at each stage.
- (2) The law governing  $|S| \geq 1$  and  $0 < |S| < 1$  can be designed separately, so their parameters do not affect each other.
- (3) Two parameters,  $k_1$  and  $k_3$ , are added, making parameter adjustment more flexible.

Theoretically, it can be proven that the proposed piecewise power reaching law has the following two properties in terms of convergence time.

**Property 1.** Let the initial value of  $S$  be  $S_0$ . A system using the piecewise power reaching law will reach the sliding surface in finite time, given by:

$$t = \begin{cases} t_1 + t_2 & |S_0| \geq 1 \\ t_3 & |S_0| < 1 \end{cases} \tag{23}$$

where

$$t_1 = \frac{q}{k_1(p-q)} \left[ \ln(k_1 + k_2) - \ln\left(k_1 S_0^{\frac{q-p}{q}} + k_2\right) \right] \tag{24}$$

$$t_2 = \frac{n}{k_3(m-n)} [\ln(k_3 + k_4) - \ln k_4] \tag{25}$$

$$t_3 = \frac{n}{k_3(m-n)} \left[ \ln\left(k_3 S_0^{\frac{n-m}{n}} + k_4\right) - \ln k_4 \right] \tag{26}$$

**Proof.** If  $|S_0| \geq 1$ , the reaching process is divided into two phases:  $|S|$  moves from  $|S_0|$  to 1 and then from 1 to 0.

When  $1 \leq |S| < |S_0|$ :

$$\dot{S} + k_1 S + k_2 S^{\frac{p}{q}} = 0 \tag{27}$$

Equation (26) is a Bernoulli differential equation, with a solution given by:

$$S^{\frac{q-p}{q}} = C e^{k_1(\frac{p-q}{q})t} - \frac{k_2}{k_1} \tag{28}$$

where  $C = S_0^{\frac{q-p}{q}} + \frac{k_2}{k_1}$ . Since  $p$  and  $q$  are both odd,  $p - q$  is even, and  $S_0^{\frac{q-p}{q}} = (-S_0)^{\frac{q-p}{q}}$ .

Let  $S = \pm 1$ , then the following expression is obtained:

$$t_1 = \frac{q}{k_1(p-q)} \left[ \ln(k_1 + k_2) - \ln\left(k_1 S_0^{\frac{q-p}{q}} + k_2\right) \right] \tag{29}$$

When  $0 < |S| < 1$ :

$$\dot{S} + k_3 S + k_4 S^{\frac{m}{n}} = 0 \tag{30}$$

Following a similar solution process, where  $S_0 = \pm 1$ , and let  $S = 0$ ; then, the following expression is obtained:

$$t_2 = \frac{n}{k_3(m-n)} [\ln(k_4) - \ln(k_3 + k_4)] \tag{31}$$

Therefore, the time required to reach the sliding surface is  $t_1 + t_2$ .

If  $0 < |S_0| < 1$ , then the approaching process consists of only one phase, where  $S$  moves from  $S_0$  to 0.



Similarly, the following is derived:

$$t_3 = \frac{n}{k_3(m-n)} \left[ \ln k_4 - \ln \left( k_3 S_0^{\frac{n-m}{n}} + k_4 \right) \right] \tag{32}$$

□.

**Property 2.** *The convergence time  $t$  has a maximum value independent of  $S_0$ . Specifically, systems using the piecewise power reaching law (22) will reach the sliding surface within a fixed time.*

**Proof.** If  $|S_0| \geq 1$ , the convergence time is  $t = t_1 + t_2$ , where  $t_2$  is already independent of  $S_0$ . Hence, we only need to prove that  $t_1$  has a maximum value that is independent of  $S_0$ .

According to the inequality  $\ln(x) \leq x - 1$ ,

$$\begin{aligned} t_1 &= \frac{q}{k_1(p-q)} \left[ \ln(k_1 + k_2) - \ln \left( k_1 S_0^{\frac{q-p}{q}} + k_2 \right) \right] \leq \frac{q}{k_1(p-q)} \left( \frac{k_1 + k_2}{k_1 S_0^{\frac{q-p}{q}} + k_2} - 1 \right) \\ &= \frac{q \left( 1 - S_0^{\frac{q-p}{q}} \right)}{(p-q) \left( k_1 S_0^{\frac{q-p}{q}} + k_2 \right)} < \frac{q}{k_2(p-q)} \end{aligned} \tag{33}$$

Therefore,

$$t < \frac{q}{k_2(p-q)} + \frac{n}{k_3(m-n)} [\ln(k_3 + k_4) - \ln k_4] \tag{34}$$

If  $S_0 < 1$ ,

$$t = t_3 = \frac{n}{k_3(m-n)} \left[ \ln k_4 - \ln \left( k_3 S_0^{\frac{n-m}{n}} + k_4 \right) \right] \leq \frac{n}{k_3(m-n)} \frac{-k_3 S_0^{\frac{n-m}{n}}}{k_3 S_0^{\frac{n-m}{n}} + k_4} < \frac{n}{k_3(n-m)} \tag{35}$$

In summary, the convergence time  $t$  has a maximum value independent of  $S_0$ . □

By replacing the traditional constant-velocity reaching law with the aforementioned piecewise power reaching law, we obtain the structure of the controller as follows:

$$u_c = \begin{cases} \Gamma(\cdot) - J \left[ k_1 S + k_2 |S|^{\frac{p}{q}} \text{sgn}(S) \right] - k \dot{q}_{ev} & |S| \geq 1 \\ \Gamma(\cdot) - J \left[ k_3 S + k_4 |S|^{\frac{m}{n}} \text{sgn}(S) \right] - k \dot{q}_{ev} & |S| < 1 \end{cases} \tag{36}$$

### 5.3. The Influence of Parameters on the Convergence Rate

From the expression of the convergence rate, increasing  $k_1, k_2, k_3, k_4$ , and  $\frac{p}{q}$  and decreasing  $\frac{m}{n}$  will both increase the convergence rate. However, the excessive pursuit of an increase in convergence rate will increase the control torque, which is not conducive to the stable control of the spacecraft. Due to the independent design of  $\frac{p}{q}$  and  $\frac{m}{n}$ , appropriate adjustments can be made based on the control effect. The following focuses on analyzing the impact of the four variables with constraint relationships,  $k_1, k_2, k_3$  and  $k_4$  on the convergence rate.

When  $|S| > 1$ , increase  $k_1$  and  $k_2$  by  $\lambda (\lambda > 0)$ , respectively, and the convergence rates become the following:

$$\dot{S}_1 = -k_1 S - k_2 S^{\frac{p}{q}} - \lambda S \tag{37}$$

$$\dot{S}_2 = -k_1 S - k_2 S^{\frac{p}{q}} - \lambda S^{\frac{p}{q}} \tag{38}$$

Due to  $|S| > 1$  and  $\frac{p}{q} > 1$ ,  $|\dot{S}_2| > |\dot{S}_1|$ . Increasing  $k_2$  is more conducive to increasing the convergence rate.

When  $0 < |S| < 1$ , increase  $k_3$  and  $k_4$  by  $\lambda (\lambda > 0)$ , respectively, and the convergence rates become the following:

$$\dot{S}_3 = -k_3 S - k_4 S^{\frac{m}{n}} - \lambda S \tag{39}$$

$$\dot{S}_4 = -k_3 S - k_4 S^{\frac{m}{n}} - \lambda S^{\frac{m}{n}} \tag{40}$$

Due to  $0 < |S| < 1$  and  $0 < \frac{m}{n} < 1$ ,  $|\dot{S}_4| > |\dot{S}_3|$ . Increasing  $k_4$  is more conducive to increasing the convergence rate.

In summary, in order to increase the convergence rate, priority should be given to increasing  $k_2$  and  $k_4$ , while  $k_1$  and  $k_3$  are used to ensure constraints.

### 6. Simulation Experiments and Analysis

Numerical simulations were conducted for the designed controller to verify the effectiveness of the control methods described above. Due to the need for the three-axis stable control of satellites, a large torque output is required in the rolling axis direction. Therefore, a scissor-configuration CMG is installed in the rolling axis direction, and flywheels are installed on the other two axes, as shown in Figure 4. The performance parameters of CMG and the flywheel are shown in Tables 1 and 2.

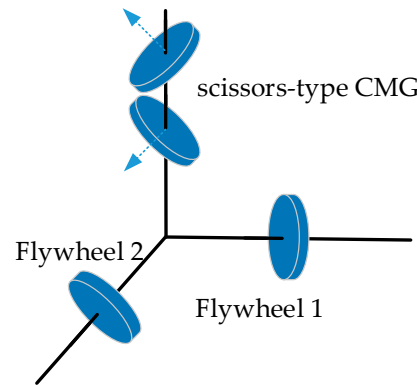


Figure 4. Satellite actuator configuration.

Table 1. Parameters of CMG.

Parameter	Value
Maximum Output Torque/(N · m)	6
Angular Momentum (Nms)	0.5
Rotational Inertia $J_w$ /(kg · m <sup>2</sup> )	0.025

Table 2. Parameters of flywheel.

Parameter	Value
Maximum Output Torque/(N · m)	0.2
Angular Momentum (Nms)	0.2
Rotational Inertia $J_w$ /(kg · m <sup>2</sup> )	0.01

The rotational inertia of the microsatellite is as follows:

$$J = \begin{bmatrix} 6 & 0 & 0 \\ 0 & 5 & 0 \\ 0 & 0 & 7 \end{bmatrix} (\text{kg} \cdot \text{m}^2)$$

The satellite is allowed a maximum rotational speed of  $8^\circ/\text{s}$  and a maximum angular acceleration of  $10^\circ/\text{s}^2$ . Controller parameters are selected as  $k = 0.005$ ,  $k_1 = 5$ ,  $k_2 = 0.1$ ,  $k_3 = 3$ ,  $k_4 = 2.1$ ,  $\frac{p}{q} = \frac{5}{3}$ , and  $\frac{m}{n} = \frac{5}{7}$ .

The microsatellite undergoes three sequential large-angle maneuvers. Specifically, it starts with an initial attitude of  $(0, 0, 0)$  rad and an angular velocity of  $(0, 0, 0)$  rad/s. In the first maneuver, it moves to a desired attitude of  $(0, 0, \frac{\pi}{4})$  rad and holds this position for 5 s. Following this, in the second maneuver, it shifts to another desired attitude  $(0, \frac{\pi}{6}, -\frac{\pi}{6})$  rad, holding again for 5 s. In the third and final maneuver, it transitions to the desired attitude  $(\frac{\pi}{6}, \frac{\pi}{6}, \frac{\pi}{3})$  rad with a desired angular velocity of  $(0, 0, 0)$  rad/s. Without external disturbances, the spacecraft's desired and actual attitudes are illustrated in Figures 5–8.

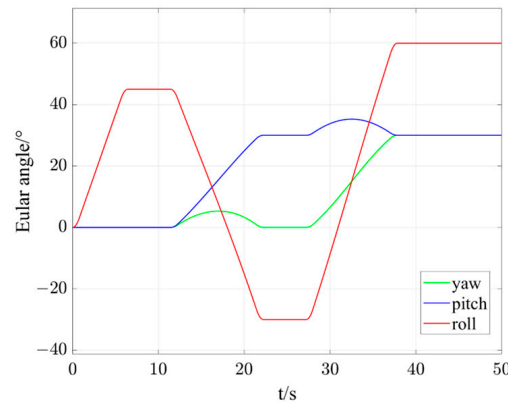


Figure 5. Desired Euler angles.

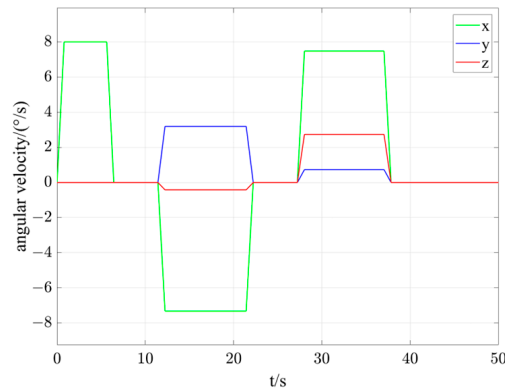


Figure 6. Desired angular velocity.

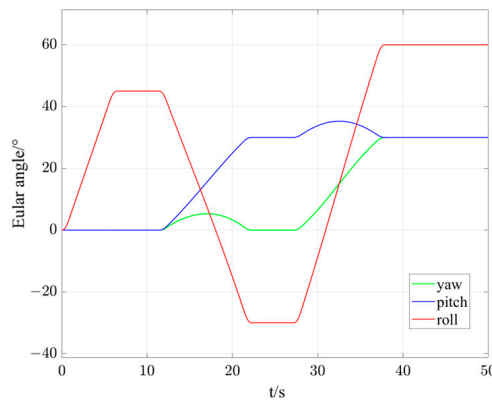
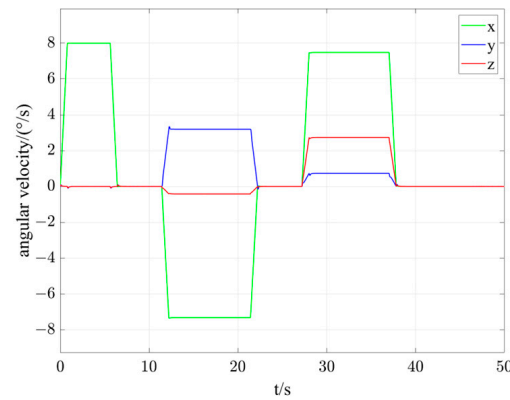


Figure 7. Actual Euler angles.



**Figure 8.** Actual angular velocity.

Figures 5–8 highlight that the spacecraft’s attitude almost aligns with its desired attitude. A minor fluctuation occurs when the angular velocity changes cease, resulting from a sudden change in the satellite’s state. The controller cannot immediately track this change and requires a brief period to converge. However, as inferred from Figure 8, this convergence time is quite short. Such transient behaviors do not significantly impact the satellite’s control performance and fall within acceptable limits. This suggests that the designed controller can effectively manage the spacecraft during large-angle maneuvering observation tasks.

Simulations were conducted to compare the performance of the proposed controller with the conventional power reaching law, which is defined as follows:

$$\dot{S} = -5|S|^{\frac{5}{3}}\text{sgn}(S) - 0.1|S|^{\frac{1}{3}}\text{sgn}(S) \tag{41}$$

Figures 9–12 depict the Euler angle control precision and angular velocity control precision during large-angle attitude maneuvers using two distinct reaching laws. Figures 13 and 14 present the control torque comparisons for these reaching laws.

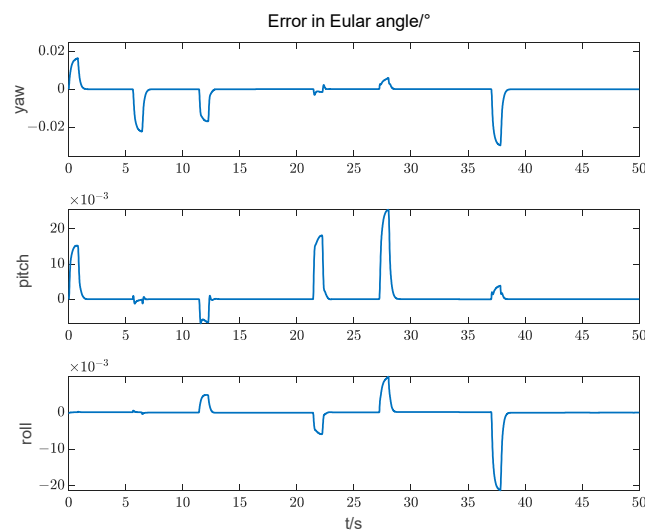


**Figure 9.** Error in Euler angles of the piecewise power reaching law.

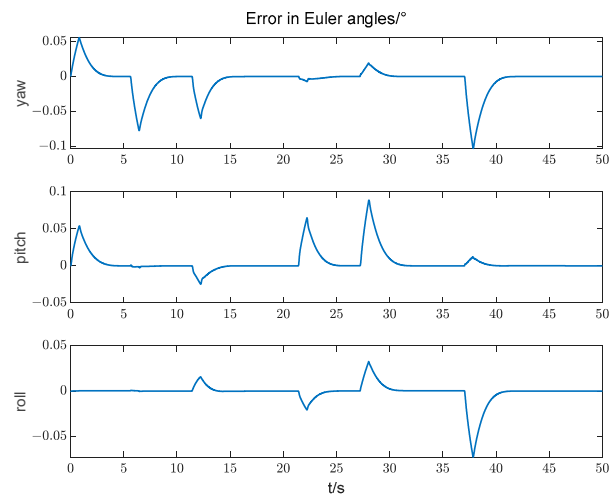


Figure 10. Error in Euler angles of the conventional power reaching law.

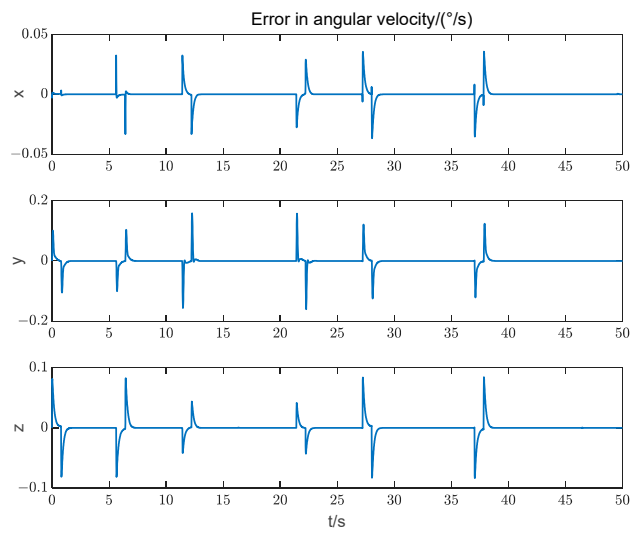


Figure 11. Error in angular velocity of the piecewise power reaching law.

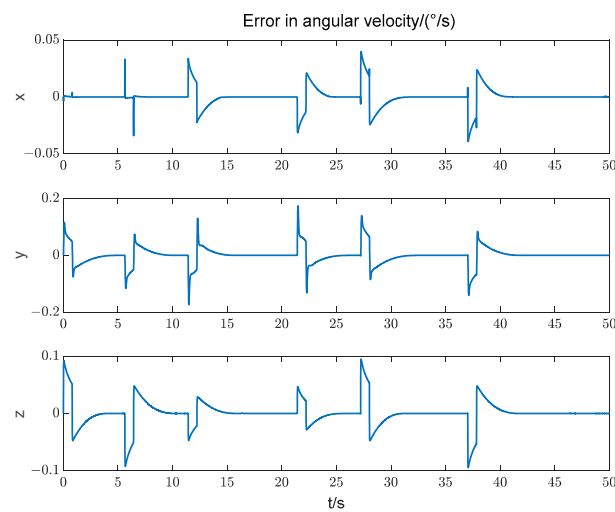
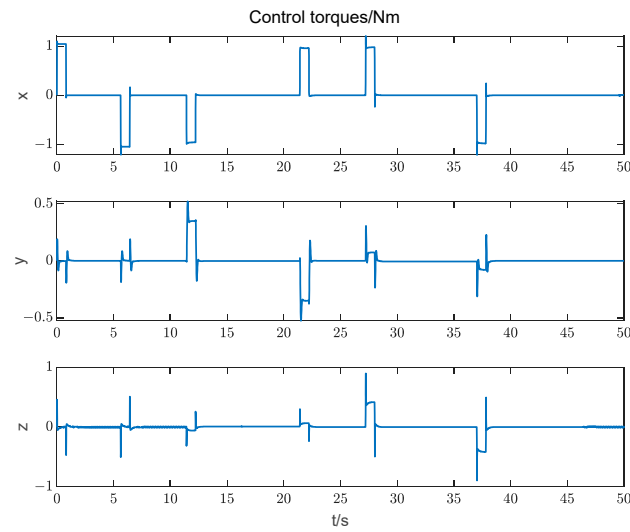
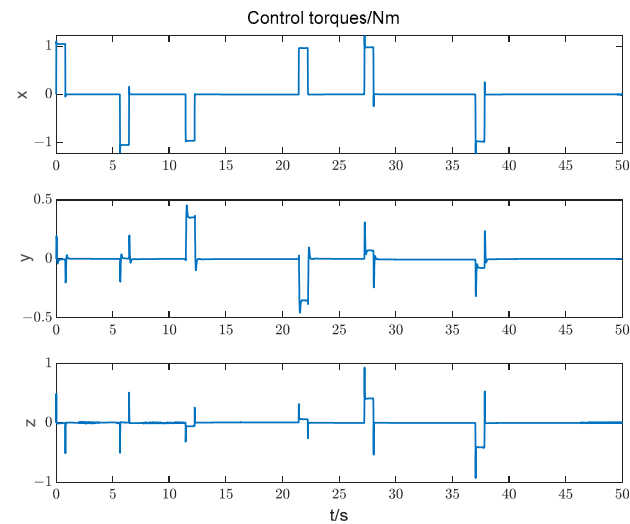


Figure 12. Error in angular velocity of the conventional power reaching law.



**Figure 13.** Control torques of the piecewise power reaching law.



**Figure 14.** Control torques of the conventional power reaching law.

Figures 9 and 10 reveal that throughout the spacecraft's observation task, there is an amplification in Euler angle and angular velocity errors during the satellite's acceleration or deceleration phases, primarily due to controller delays. The attitude control algorithm based on the conventional power reaching law converges around 5 s, with the Euler angle error reaching up to  $0.1^\circ$ . In contrast, based on the segmented power reaching law, the developed attitude control algorithm can converge within 2 s, with a maximum error of  $0.03^\circ$ . Compared to the conventional power reaching law, there is a reduction in convergence time by approximately 3 s and a 70% improvement in control accuracy. This underscores the rapid convergence and high-precision advantages of the controller designed in this paper.

Figures 11 and 12 highlight that the angular velocity control precision of both reaching law-based attitude control algorithms is comparable and around  $0.15^\circ/\text{s}$ . However, due to the longer convergence time of the conventional power reaching law's attitude control algorithm, the impact from its angular velocity control error is relatively significant, which is the primary cause for the increased Euler angle error.

Figures 13 and 14 indicate that the torque of both reaching law-based attitude control algorithms is approximately 1 Nm. Both are within the output torque range of the actuating mechanism and meet the design requirements.

## 7. Conclusions

This study considered the requirements of agile attitude maneuvers for multi-target observations using microsatellites. It developed a novel segmented power reaching law, and an attitude maneuver scheme was designed, effectively addressing the attitude maneuver control problem for multi-target observations by low-Earth-orbit microsatellites during short arc segments. The following conclusions were drawn from the research:

1. The proposed piecewise power-law convergence law can converge to the sliding mode surface in finite time, and there exists a maximum value independent of the initial state at that time.
2. Increasing  $k_1$ ,  $k_2$ ,  $k_3$ , and  $k_4$  will increase the convergence rate of the system, but  $k_3$  and  $k_4$  have a greater impact on the convergence rate.
3. Compared to conventional power-law attitude control algorithms, attitude control algorithms based on the segmented power-law approach have a faster convergence time and higher control accuracy. Under the simulation conditions in this study, the convergence time was reduced by about 3 s, and the control accuracy was improved by about 70%.

**Author Contributions:** Formal analysis, L.L.; Investigation, X.Y.; Software, Y.L.; Validation, Z.L. All authors have read and agreed to the published version of the manuscript.

**Funding:** This research received no external funding.

**Institutional Review Board Statement:** Not applicable.

**Informed Consent Statement:** Not applicable.

**Data Availability Statement:** The data presented in this study is available on request from the corresponding author. The data are not publicly available due to privacy.

**Conflicts of Interest:** The authors declare no conflicts of interest.

## References

1. Su, Y.; Zheng, C. A new nonsingular integral terminal sliding mode control for robot manipulators. *Int. J. Syst. Sci.* **2020**, *51*, 1418–1428. [[CrossRef](#)]
2. Vafaei, H.A.A.J. Synchronization of fractional-order chaotic systems with disturbances via novel fractional-integer integral sliding mode control and application to neuron models. *Math. Methods Appl. Sci.* **2019**, *42*, 2761–2773. [[CrossRef](#)]
3. Ye, D.; Zou, A.M.; Sun, Z. Predefined-Time Predefined-Bounded Attitude Tracking Control for Rigid Spacecraft. *IEEE Trans. Aerosp. Electron. Syst.* **2022**, *58*, 464–472. [[CrossRef](#)]
4. Liu, Y.; Jiang, B.; Lu, J.; Cao, J.; Lu, G. Event-Triggered Sliding Mode Control for Attitude Stabilization of a Rigid Spacecraft. *IEEE Trans. Syst. Man Cybern. Syst.* **2018**, *50*, 3290–3299. [[CrossRef](#)]
5. Zhu, Y.; Qiao, J.; Guo, L. Adaptive Sliding Mode Disturbance Observer-Based Composite Control With Prescribed Performance of Space Manipulators for Target Capturing. *IEEE Trans. Ind. Electron.* **2018**, *66*, 1973–1983. [[CrossRef](#)]
6. Shao, K.; Zheng, J.; Huang, K.; Wang, H.; Man, Z.; Fu, M. Finite-Time Control of a Linear Motor Positioner Using Adaptive Recursive Terminal Sliding Mode. *IEEE Trans. Ind. Electron.* **2020**, *67*, 6659–6668. [[CrossRef](#)]
7. Wang, Y.; Feng, Y.; Zhang, X.; Liang, J. A New Reaching Law for Antidisturbance Sliding-Mode Control of PMSM Speed Regulation System. *IEEE Trans. Power Electron.* **2020**, *35*, 4117–4126. [[CrossRef](#)]
8. Herrmann, G.; Spurgeon, S.K.; Edwards, C. On robust, multi-input sliding-mode based control with a state-dependent boundary layer. *J. Optim. Theory Appl.* **2006**, *129*, 89–107. [[CrossRef](#)]
9. Yu, X.; Zhihong, M. Multi-input uncertain linear systems with terminal sliding-mode control. *Automatica* **1998**, *34*, 389–392. [[CrossRef](#)]
10. Feng, Y.; Han, F.; Yu, X. Chattering free full-order sliding-mode control. *Automatica* **2014**, *50*, 1310–1314. [[CrossRef](#)]
11. Hou, H.; Yu, X.; Xu, L.; Rsetam, K.; Cao, Z. Finite-Time Continuous Terminal Sliding Mode Control of Servo Motor Systems. *IEEE Trans. Ind. Electron.* **2020**, *67*, 5647–5656. [[CrossRef](#)]
12. Van, M. Higher-order terminal sliding mode controller for fault accommodation of Lipschitz second-order nonlinear systems using fuzzy neural network. *Appl. Soft Comput.* **2021**, *104*, 107186. [[CrossRef](#)]
13. Pukdeboon, C.; Zinober, A.S.; Thein, M.W.L. Quasi-Continuous Higher Order Sliding-Mode Controllers for Spacecraft-Attitude-Tracking Maneuvers. *IEEE Trans. Ind. Electron.* **2010**, *57*, 1436–1444. [[CrossRef](#)]
14. Lu, K.; Xia, Y.; Zhu, Z.; Basin, M.V. Sliding mode attitude tracking of rigid spacecraft with disturbances. *J. Frankl. Inst.* **2012**, *349*, 413–440. [[CrossRef](#)]

15. Gao, S.; Jing, Y.; Liu, X.; Zhang, S. Finite-time attitude-tracking control for rigid spacecraft with actuator failures and saturation constraints. *Int. J. Robust Nonlinear Control*. **2019**, *30*, 1903–1937. [[CrossRef](#)]
16. Wu, Y.D.; Wu, S.F.; Gong, D.R.; Kang, Z.Y.; Wang, X.L. Spacecraft Attitude Maneuver Using Fast Terminal Sliding Mode Control Based on Variable Exponential Reaching Law. In Proceedings of the International Conference on Aerospace System Science and Engineering, Toronto, ON, Canada, 30 July–1 August 2019; Springer: Singapore, 2019. [[CrossRef](#)]
17. Wang, C.; Xia, H.; Wang, Y.; Ren, S. Discrete-time Sliding Mode Control with Adaptive Reaching Law via Implicit Euler Method. *Int. J. Control Autom. Syst.* **2023**, *21*, 109–116. [[CrossRef](#)]
18. Ma, H.; Xiong, Z.; Li, Y.; Liu, Z. Sliding Mode Control for Uncertain Discrete-Time Systems using An Adaptive Reaching Law. *IEEE Trans. Circuits Syst. II Express Briefs* **2020**, *68*, 722–726. [[CrossRef](#)]
19. Panathula, C.B.; Rosales, A.; Shtessel, Y.B.; Fridman, L.M. Closing Gaps for Aircraft Attitude Higher Order Sliding Mode Control Certification via Practical Stability Margins Identification. *IEEE Trans. Control Syst. Technol.* **2017**, *26*, 2020–2034. [[CrossRef](#)]
20. Zhang, H.X.; Fan, J.S.; Meng, F.; Huang, J.F. A new double power reaching law for sliding mode control. *Control Decis.* **2013**, *28*, 289–293.
21. Zhang, Y.; Ma, G.F.; Guo, Y.N.; Zeng, T.Y. A multipower reaching law of sliding mode control design and analysis. *Acta Autom. Sin.* **2016**, *42*, 466–472.
22. Ming, P.; Tao, J.; Kechang, F. Finite time stable chattering-free reaching law design with bounded input. *Control. Decis.* **2018**, *33*, 135–142.
23. Wang, H.G.; Wu, G.Q.; Bai, T. Integrated Disturbance Observer Attitude Controller for a Satellite with Rotating Solar Array. In Proceedings of the 4th International Conference on Electrical, Automation and Mechanical Engineering, Beijing, China, 21–22 June 2020.

**Disclaimer/Publisher’s Note:** The statements, opinions and data contained in all publications are solely those of the individual author(s) and contributor(s) and not of MDPI and/or the editor(s). MDPI and/or the editor(s) disclaim responsibility for any injury to people or property resulting from any ideas, methods, instructions or products referred to in the content.